Geochemical calibration for carbonate clay caprock under acidic conditions: experimental and numerical insights

Geochemical calibration for carbonate clay caprock under acidic conditions: experimental and numerical insights

Vincenzo Sergio Vespo[1,*], Liliana Gramegna[2], Adriano Fiorucci[3], Gabriele Della Vecchia[2], Guido Musso[1]

[1] Department of Structural, Geotechnical and Building Engineering, Politecnico di Torino, 10129, Turin, Italy

[2] Department of Civil and Environmental Engineering, Politecnico di Milano, 20133, Milan, Italy

[3] Department of Environment, Land and Infrastructure Engineering, Politecnico di Torino, 10129, Turin, Italy

[*] corresponding author vincenzosergio.vespo@polito.it

Abstract

Accurate prediction of possible chemo-mechanical effects on the behaviour of caprocks interacting with CO_2 in geological storage operations requires developing models coupling reactive transport and mechanical processes. Determination of the geochemical model parameters is critical to this extent. This work refers to the case of a carbonate clay caprock, where a novel procedure aimed at parameter calibration was based on titration tests, accompanied by mineralogical and chemical analyses. Depending on the value of the equilibrium constants, a competing behaviour between calcite and dolomite dissolution was outlined. The obtained model parameters were used in the simulation of tests where oedometer samples were exposed to acidic solution through diffusion and advection. The simulations were found to provide satisfactory results, helping to assess the specific role of the two carbonates dissolution on the accumulated strains. The advection test was found to be compatible with larger carbonates dissolution characterized by sharp gradients of volumetric fractions, whereas the diffusion test was compatible with smaller carbonates dissolution extending on larger areas with smoother volumetric fractions gradients.

Keywords: Geochemical model, carbonate clay caprock, CO_2 storage, carbonates dissolution/precipitation, reactive transport, acidic exposure tests, UN SDG 13

1 Introduction

Long-term storage of CO_2 in geological formations requires that the overlying caprock provides a reliable seal to prevent preferential pathways. The latter might develop through faults or abandoned wells, but CO_2 leakage may also occur because of shear failure (e.g. Vilarrasa et al., 2013) or desaturation of caprock (e.g. Vespo et al., 2024). These phenomena might be exacerbated by microstructure and mineralogy changes due to geochemical reactions triggered by pore fluid acidification induced by CO_2 dissolution (Ciancimino et al., 2025; Vespo et al., 2025), which can bring the pH ≅ 3 (Liu et al., 2022).

Carbonate caprocks are particularly sensitive, as calcite and dolomite readily react with acidified water. Predicting reaction effects requires robust reactive transport models highly sensitive to parameters such as minerals equilibrium constants and reactive specific surfaces, largely dependent on mineralogy, fabric and environmental conditions. Focusing on a carbonate clay caprock, this study proposes parameter calibration through controlled titration experiments. The reactive transport model was then validated against experimental tests where reconstituted specimens were exposed to an acidic solution (10^{-3} M HCl).

2 Reactive transport model for carbonate dissolution

The reactive transport model of Lopez-Vizcaino et al. (2021) was implemented in COMSOL Multiphysics by Gramegna et al. (2023). The modelling approach, here proposed in one dimensional condition, is divided into two stages. Chemical speciation is first solved (using PHREEQ-C) to obtain the initial equilibrium concentration of all the chemical species. Then, the mass balance equations for water (Eq. 1) and dissolved species (Eq. 2) are integrated in space and time:

$$\frac{\partial \phi \rho_{sol}}{\partial t} + \frac{\partial \rho_{sol} q}{\partial z} = 0 \qquad \textit{Eq. 1}$$

$$\frac{\partial \phi c_i}{\partial t} + \frac{\partial \rho_d c_{ad,i}}{\partial t} + \frac{\partial}{\partial z}\left(-D_{e,i}\frac{\partial c_i}{\partial z}\right) + q\frac{\partial c_i}{\partial z} = R_i + \Gamma_i \qquad \textit{Eq. 2}$$

where ϕ is the porosity, ρ_{sol} is the solution density, q is the Darcy velocity of the solution, c_i is the species concentration, ρ_d is the dry density of the caprock, $c_{ad,i}$ is the species adsorbed concentration, $D_{e,i}$ is the species effective diffusion coefficient, R_i is the species total reaction rate, and Γ_i is the species sink/source term.

If chemical equilibrium between aqueous species is assumed, it is convenient, from the numerical point of view, to reduce the number of independent concentrations. In a system containing N aqueous

species, the number of independent chemical components N_p (primary species) is reduced from N by the N_s linearly dependent chemical reactions:

$$N_p = N - N_s \qquad \textit{Eq. 3}$$

In the following, the subscript α (with ranging from 1 to N_p) refers to the N_p primary species, while the subscript β (ranging from 1 to N_s) refers to the N_s secondary species. The reversible chemical reactions between the primary and the secondary species take the classical form of equilibrium chemical reactions:

$$A_\beta \rightleftharpoons \sum_{\alpha=1}^{N_p} \nu_{\beta\alpha} A_\alpha \qquad \textit{Eq. 4}$$

where A_β and A_α are chemical formulas of the secondary species β and of the primary species α, and $\upsilon_{\beta\alpha}$ is the stoichiometric coefficient of the primary species α in a reversible aqueous reaction with the secondary species β. In the following, the dissolved primary species are: H^+, Ca^{2+}, Mg^{2+}, Cl^-, SO_4^{2-}.

The reversible reactions provide an algebraic link between the primary and secondary species, via the law of mass action for each reaction. The activity $a_{s\beta}$ of the secondary species β is related to the activities $a_{p\alpha}$ of the primary species α as:

$$K_{eq} = a_{s\beta} \prod_{\alpha=1}^{N_p} a_{p\alpha}{}^{\nu_{\beta\alpha}} \qquad \textit{Eq. 5}$$

Where K_{eq} is the reaction equilibrium constant.

The chemical activities $a_{p\alpha}$ and $a_{s\beta}$ are in general defined as:

$$a = \gamma \frac{c}{c^\theta} \qquad \textit{Eq. 6}$$

where c^θ is a standard concentration equal to 1 mol/L and γ is the activity coefficient.

Adsorption of H^+ on the surface of phyllosilicates, which reduces the amount of H^+ free to flow and react with carbonates, was implemented via the Langmuir (1916) adsorption isotherm:

$$c_{ad,H^+} = c_{ad_{max},H^+} \frac{K_L c_{H^+}}{1 + K_L c_{H^+}} \qquad \textit{Eq. 7}$$

where c_{H^+} is the H^+ water concentration, $c_{ad_{max},H^+} = 0.52$ (mol/g) is the maximum H^+ adsorbed concentration, K_L = 14 (m^3/mol) is the Langmuir constant (values from Farrah & Pickering, 1979). Adsorption of other ions is neglected.

Consistently with the experiments, performed at atmospheric conditions, the maximum concentration of dissolved CO_2, i.e. $H_2CO_3^*$ ($H_2CO_3^* = CO_{2(aq)} + H_2CO_3$) was set as $c_{max,H_2CO_3^*} = 1.26 \cdot 10^{-8} (mol/m^3)$, higher concentrations leading to volatilization.

The effective diffusion coefficient for each primary species was expressed via the Fick law:

$$D_{e,i} = \frac{\phi}{\tau} D_i \qquad \textit{Eq. 8}$$

where D_i is the free electrolyte diffusivity for each species (Parkhurst & Appelo, 2013), $\tau = \phi^{-1/3}$ is the tortuosity as in Millington & Quirk (1961).

The total reaction rate of each dissolved primary species R_i is the sum of all the mineral dissolution-precipitation reactions that involve the species *i* and reads:

$$R_i = \sum_{m=1}^{N_m} \nu_{m,i} r_m S_m \qquad \textit{Eq. 9}$$

where r_m is the rate of precipitation/dissolution of mineral *m*, S_m is the reactive surface area, and $\upsilon_{m,i}$ is the stoichiometric coefficient of the species *i* in the dissolution/precipitation reaction.

Reaction pathways (Plummer et al., 1978; Pokrovsky & Schott, 2001) are reported in Table 1. The rates of precipitation/dissolution of calcite r_{CaCO_3} and dolomite $r_{CaMg(CO_3)_2}$, according to transition state theory (Palandri & Kharaka, 2004), are:

$$r_{CaCO_3} = \left(k_{CaCO_3}^{acid} \cdot a_{H^+} + k_{CaCO_3}^{neutral} + k_{CaCO_3}^{carb} \cdot a_{H_2CO_3^*}\right)\left(1 - \frac{a_{Ca^{2+}} \cdot a_{CO_3^{2-}}}{K_{eq,CaCO_3}}\right) \qquad \textit{Eq. 10}$$

$$r_{CaMg(CO_3)_2} = \left(k_{CaMg(CO_3)_2}^{acid} \cdot (a_{H^+})^{0.5} + k_{CaMg(CO_3)_2}^{neutral} + k_{CaMg(CO_3)_2}^{carb} \cdot \left(a_{H_2CO_3^*}\right)^{0.5}\right)\left(1 - \frac{a_{Ca^{2+}} \cdot a_{Mg^{2+}} \cdot \left(a_{CO_3^{2-}}\right)^2}{K_{eq,CaMg(CO_3)_2}}\right) \qquad \textit{Eq. 11}$$

where $k_{CaCO_3}^{acid}$, $k_{CaCO_3}^{neutral}$, $k_{CaCO_3}^{carb}$, $k_{CaMg(CO_3)_2}^{acid}$, $k_{CaMg(CO_3)_2}^{neutral}$, $k_{CaMg(CO_3)_2}^{carb}$ are empirical specific rates dependent on temperature (Palandri & Kharaka, 2004), a_{H^+}, $a_{H_2CO_3^*}$, $a_{Ca^{2+}}$, $a_{Mg^{2+}}$ and $a_{CO_3^{2-}}$ are species activities.

$K_{eq,CaCO_3}$ and $K_{eq,CaMg(CO_3)_2}$ are the equilibrium constants of reactions 'Eq. III' and 'Eq. VI' of Table 1, i.e.:

$$K_{eq,CaCO_3} = a_{Ca^{2+}} \cdot a_{CO_3^{2-}} \quad \textit{Eq. 12}$$

$$K_{eq,CaMg(CO_3)_2} = a_{Ca^{2+}} \cdot a_{Mg^{2+}} \cdot a_{CO_3^{2-}}{}^2 \quad \textit{Eq. 13}$$

The reaction rates allow calculating the rate change of calcite and dolomite volume fractions ($\dot{\phi}_{CaCO_3}$and $\dot{\phi}_{CaMg(CO_3)_2}$):

$$\dot{\phi}_{CaCO_3} = -r_{CaCO_3} \cdot S_{CaCO_3} \cdot V_{m,CaCO_3} \cdot \phi_{CaCO_3} \quad \textit{Eq. 14}$$

$$\dot{\phi}_{CaMg(CO_3)_2} = -r_{CaMg(CO_3)_2} \cdot S_{CaMg(CO_3)_2} \cdot V_{m,CaMg(CO_3)_2} \cdot \phi_{CaMg(CO_3)_2} \quad \textit{Eq. 15}$$

where $V_{m,CaCO_3}$ and $V_{m,CaMg(CO_3)_2}$ are the molar volumes.

By assuming negligible volumetric strains, the rate change of porosity is:

$$\dot{\phi} = -\dot{\phi}_{CaMg(CO_3)_2} - \dot{\phi}_{CaCO_3} \quad \textit{Eq. 16}$$

This change in porosity - induced by chemical reactions - in turn affects the storage term of the mass balance equations for water (Eq. 1) and dissolved species (Eq. 2), resulting in a coupled chemo-hydraulic process.

3 Geochemical calibration

3.1 Titration tests

The reactive transport model introduced in Section 2 requires the values of equilibrium constants and reactive specific surfaces of calcite and dolomite. Equilibrium constants cannot be reliably estimated a priori, being dependent on temperature, pore fluid composition and mineral structure; while reactive specific surfaces are material dependent, through grain size and shape.

A novel calibration procedure, based on titration tests and mineralogical/chemical analyses, was set up for a carbonate clay (CC) caprock composed of 49% carbonates (30% calcite, 19% dolomite), 29% phyllosilicates (15% illite, 14% muscovite), 15% quartz, 2% albite and 5% gypsum (Vespo, 2024). Two titration test series were performed: T1, with limited acid addition, dissolving mainly calcite; T2, with higher acid dosage, enabling also dolomite dissolution. In each test, 10 g of oven-dried CC powder were suspended and magnetically stirred in 50 mL of H_2O. HCl (12.07 M) was added incrementally in

0.3-0.6 mL steps. pH was recorded 10 minutes after each addition. T1 received 3.6 mL total acid; T2 received 7.8 mL.

Mineralogical changes were assessed by X-Ray Diffraction (XRD) with Rietveld refinement. Supernatants, filtered through 0.45 μm PTFE membranes after 48 h of sedimentation, were chemically analysed using ion chromatography (Metrohm 883) and atomic absorption spectroscopy (contrAA 800). Due to short test duration (max 4 h) and room temperature (21 °C), only carbonate reactions were expected (Gaus, 2010).

Initial suspension pH was 8.5, with carbonate volume fractions $\phi_{CaCO_3} = 0.020$ and $\phi_{CaMg(CO_3)_2} = 0.012$. Supernatant analysis showed a sulphate concentration of 2.57 g/L, consistent with complete gypsum dissolution. SO_4^{2-}, H^+, Cl^-, Ca^{2+}, and Mg^{2+} concentrations, were provided as an input for PHREEQ-C in order to obtain the initial concentrations of the other chemical species involved. Titration tests were simulated using the 1D model described in Section 2, with an initial porosity of 0.93 and a length of 2.73 cm (height of the suspension inside the beaker). Acid additions were implemented as H^+ and Cl^- sources uniformly distributed all along the domain. No advective/diffusive fluxes were included, and no-flow boundaries were imposed for all species.

3.2. Equilibrium constants estimation

Equilibrium constants for calcite and dolomite were estimated by numerically fitting the results of XRD analyses performed 48 hours after the completion of the titration tests, a timeframe that - according to the numerical simulations - ensures geochemical equilibrium. For test T1, the calcite fraction decreased to $\phi_{CaCO_3} = 0.005$ (Fig. 1(a)), while the dolomite fraction increased to $\phi_{CaMg(CO_3)_2} = 0.013$ (Fig. 1(b)). This procedure is justified by the fact that the mass of dissolved or precipitated mineral at equilibrium depends solely on the equilibrium constant (Eq. 12 and Eq. 13). Based on literature data, $K_{eq,CaCO_3}$ was varied within the range $2.8 \cdot 10^{-9} \div 8.7 \cdot 10^{-9}$ (Lide, 1995), while $K_{eq,CaMg(CO_3)_2}$ was varied between $3.2 \cdot 10^{-17}$ and $4.7 \cdot 10^{-20}$ (Sherman & Barak, 2000).

It is worth noting that the reactions involving calcite influence those involving dolomite and vice versa, because the two minerals share common ionic species (Table 1). This coupling is expected, as Eq. 12 and Eq. 13 both depend on the equilibrium activities of calcium and carbonate ions; therefore the dissolution behaviour of the two minerals is intrinsically coupled in a calcite–dolomite system. Increasing the $K_{eq,CaCO_3}$ value promotes calcite dissolution while suppressing dolomite dissolution (Fig. 1(a), (b), and Table 2, cases A, C, E). The opposite occurs when $K_{eq,CaMg(CO_3)_2}$ is increased (Fig. 1(a), (b), and Table 2, cases B, C, D). The best individual fit for calcite was obtained in case A, and for dolomite in case F.

A double-objective optimization was then performed using the root mean square error RMSE as the metric, $RMSE = \sqrt{\frac{\left(\phi_{CaCO_3,num} - \phi_{CaCO_3,exp}\right)}{2} + \frac{\left(\phi_{CaMg(CO_3)_2,num} - \phi_{CaMg(CO_3)_2,exp}\right)}{2}}$, where $\phi_{CaCO_3,num}$ and $\phi_{CaMg(CO_3)_2,num}$ are the numerically predicted volumetric fractions, and $\phi_{CaCO_3,exp}$ and $\phi_{CaMg(CO_3)_2,exp}$ are the experimental values. This procedure yielded the optimal pair of equilibrium constants for the caprock under study, namely $K_{eq,CaCO_3} = 5.8 \cdot 10^{-9}$, $K_{eq,CaMg(CO_3)_2} = 3.2 \cdot 10^{-18}$ (corresponding to case C).

Mineralogical analysis after T2 confirmed complete dissolution of both calcite and dolomite, consistent with a stoichiometric requirement of 0.009 mol H^+/g (moles of H^+ added per gram of solids). This aligns with measured Ca^{2+} and Mg^{2+} concentrations in the supernatant ($Ca^{2+} \approx 43.13$ g/L; $Mg^{2+} \approx 6.52$ g/L).

3.3 Reactive specific surfaces estimation

The reactive specific surfaces were estimated through a back-analysis of the titration curves, while keeping the equilibrium constants obtained in Section 3.2 fixed. The titration curves in Fig. 2 -expressed as moles of H^+ added per gram of solids - are based on pH measurements taken 10 minutes after each acid addition. This interval is insufficient to reach steady-state conditions (see Fig. 1(a) and (b), where equilibrium requires approximately 48 hours) and therefore reflects the kinetics of carbonate dissolution, which depend on the reactive specific surface area.

As calcite dissolves at lower mol H^+/g values than dolomite (results of T1 and T2 tests), its reactive specific surface S_{CaCO_3} was calibrated for mol H^+/g < 0.005 (threshold for full calcite dissolution). $S_{CaMg(CO_3)_2}$ was calibrated for higher mol H^+/g values. Increasing both S_{CaCO_3} and $S_{CaMg(CO_3)_2}$ from $3 \cdot 10^4$ to $3 \cdot 10^6$ m^2/m^3 significantly improved model predictions, with no substantial gain beyond $3 \cdot 10^6$ m^2/m^3 (Fig. 2 and Table 3). Assuming spherical particles, this suggests carbonates diameters smaller than 2 μm.

Beyond the error related to the choice of the pair of equilibrium constants, discrepancies between experimental and numerical results may also arise from the presence of dolomite variants such as ankerite, where magnesium is partly replaced by iron or manganese.

4 Reactive transport tests

Reactive transport tests were conducted to assess the effects of acidic exposure on reconstituted CC specimens. The tests, carried out in oedometer under constant vertical stress, involved exposing specimens to a 10^{-3} M HCl solution (pH = 3). A Diffusion Test (DT) and an Advection Test (AT) were performed. A third test, without acidic exposure, served as a reference for creep deformation (Creep Test, CT). Specimens were reconstituted by mixing the solid phase with distilled water in slurry state.

198 Applied vertical stress was 6.3 MPa for CT and DT, and 6.4 MPa for AT. As a first approximation, the
199 stress difference of 0.1 MPa was considered to have no significant effects. Initial porosity at the start of
200 exposure was 0.31, while initial calcite and dolomite volumetric fractions were 0.206 and 0.109. Tests
201 lasted 197 days (CT), 333 days (DT), and 184 days (AT).
202 In DT, the specimen base was sealed, while the top was connected to a reservoir where a pH = 3
203 condition was restored daily, enabling H^+ diffusion towards the specimen. 0.0015 mol H^+/g were overall
204 used and the pH of the reservoir solution reverted to 6 within 24 hours after each acid addition.
205 In AT, a 10^{-3} M HCl solution was flushed through the specimen by applying 80.5 kPa/mm pressure
206 gradient. About 0.9 L of acidic solution (0.00002 mol H^+/g) were flushed through the specimen: the
207 outflow pH remained stable at ~8.3 whereas the hydraulic conductivity decreased from $3.55 \cdot 10^{-12}$ m/s
208 to $3.15 \cdot 10^{-12}$ m/s.
209 Fig. 3 shows the time evolution of vertical strain ε_v of the exposure stage (DT and AT) and of the
210 creep stage (CT). Although differences are small, at the same testing time the strain follows the order
211 ε_v (CT) < ε_v (DT) < ε_v (AT), suggesting that the dissolution caused by exposure to the acid solution
212 contributes to the vertical strain. Furthermore, AT strains were larger as the advective mechanism
213 proved to be more effective in transporting H^+ ions.

214 **4.1 Assessment of geochemical effects**

215 AT and DT were simulated using the reactive transport model of Section 2, considering a one-
216 dimensional domain of length 11.8 mm and 11.3 mm, respectively. Reactions parameters as determined
217 in Section 3 were used. Initial ionic species concentrations matched those used in the titration
218 simulations.
219 In the 1D simulations of the DT test, both the specimen and the reservoir were modelled. The latter
220 was introduced as a domain, whose length was set equal to 280 mm, equal to the ratio between the
221 volume of the reservoir (550 cm^3) and specimen cross section (19.63 cm^2). Solute flux was allowed
222 between the reservoir and the soil specimen. Daily acid additions were simulated by means of source
223 terms of H^+ and Cl^- in the reservoir, where no reactions occur. No-flow hydraulic boundary conditions
224 were applied at both model ends.
225 In the AT simulation, only the soil specimen was modelled. From the hydraulic point of view, water
226 pressure was applied at both specimen ends. Fixed 10^{-3} M H^+ and Cl^- concentrations were imposed at
227 the inlet, and free outflow at the outlet. The adopted hydraulic conductivity was set equal to
228 $K_{sol} = 3.35 \cdot 10^{-12}$ m/s.
229 Fig. 4(a), (b), (c), (d) shows good agreement between simulations and experimental results. Post-
230 mortem XRD analyses of sub-specimens trimmed from three heights revealed that chemical reactions
231 affected only part of each specimen. In AT, calcite fully dissolved and dolomite partially dissolved near
232 the inlet, confined to 0.5 mm. In DT, a broader reactive front extended on the top third, with incomplete

calcite dissolution at the reservoir interface. Dolomite dissolution was absent, while minor precipitation was observed and predicted in the upper region. The sharp front in AT results from inward transport and accumulation of reaction products (Ca^{2+}, Mg^{2+}, HCO_3^-), limiting further dissolution. In DT, products diffuse towards the reservoir, enabling deeper acid penetration and a thicker reactive zone.

The satisfactory performance of the transport model can be attributed to the fact that, although the titration-based calibration spans a wide range of concentrations, the geochemical model in Fig. 2 exhibits excellent agreement with the experimental data at low H^+/g values. These lower concentrations are those imposed in the transport tests, thereby supporting the applicability of the calibrated parameters to the simulated conditions. Simulation results also suggest that the evolution of the volumetric fraction of the carbonate species, averaged over the whole specimen in Fig. 5, depends on the transport mechanism. Advective transport of H^+ causes a roughly linear decrease of calcite with time, whereas the dolomite volumetric fraction remains almost constant. Conversely, in case of H^+ diffusion, the rate of calcite volumetric fraction dissolution reduces with time, whereas a slight precipitation of dolomite is predicted. If the comparison is made at the same exposure time, advection appears to induce a larger dissolution of total carbonates than diffusion. This is consistent with the experimentally recorded strains (Fig. 3), also larger in the advection test.

5 Conclusions

The calibration and validation of a reactive transport model for an acidic solution interacting with carbonate clays was presented. A novel titration-based approach enabled the determination of key parameters like equilibrium constants and reactive specific surfaces. The parameters obtained were then used to simulate the oedometer exposure tests under acidic conditions.

Although the transport regime and reactive surface availability differ markedly between the oedometer test (reconstituted specimen) and the titration test (powder suspension), this simplified approach nevertheless yielded good predictions of the changes in calcite and dolomite volumetric fractions. This model allows to correlate the experimentally recorded axial strain with the mineralogical evolution of the specimens, which is strongly dependent on the dominant transport mechanism (diffusion vs. advection).

This integrated modelling and calibration framework provides a robust tool for predicting mineral dissolution patterns in reactive porous media exposed to acidic solutions, such as the one generated by CO_2 dissolution. The application of the proposed framework to CO_2 sequestration shall however be performed in the laboratory at the relevant pressure and temperature conditions. Titration tests were found to provide a satisfactory evaluation of the parameters describing the geochemical reactions for the simulation of reactive transport processes in reconstituted specimens: in this context, the role of microstructural differences between the properties of the powder and those of the soil were found to be

negligible. This is a promising result also for the application of the framework to intact specimens, although experimental validation is recommended.

References

Ciancimino, A., Daka, T., Gramegna, L., Musso, G., Volonté, G., & Della Vecchia, G. (2025). A constitutive framework for caprocks accounting for viscoplastic cyclic degradation and coupled geo-chemo-mechanical processes. *Geomechanics for Energy and the Environment*, *42*, 100689.

Farrah, H., & Pickering, W. F. (1979). pH effects in the adsorption of heavy metal ions by clays. *Chemical Geology*, *25*(4), 317-326.

Gaus, I. (2010). Role and impact of CO_2–rock interactions during CO_2 storage in sedimentary rocks. *International Journal of Greenhouse Gas Control*, *4*(1), 73-89.

Gramegna, L., Musso, G., Messori, A., & Della Vecchia, G. (2023). A reactive transport model for calcite-rich caprocks in the context of geological carbon storage. Symposium on Energy Geotechnics.

Langmuir, I. (1916). The constitution and fundamental properties of solids and liquids. Part I. Solids. *Journal of the American chemical society*, *38*(11), 2221-2295.

Lide, D. R. (1995). *CRC handbook of chemistry and physics: a ready-reference book of chemical and physical data*. CRC press.

Liu, Q., Benitez, M. D., Xia, Z., & Santamarina, J. C. (2022). Pore-scale phenomena in carbon geological storage (Saline aquifers—Mineralization—Depleted oil reservoirs). *Frontiers in Energy Research*, *10*, 979573.

Lopez-Vizcaino, R., Yustres, A., Cabrera, V., & Navarro, V. (2021). A worksheet-based tool to implement reactive transport models in COMSOL Multiphysics. *Chemosphere*, *266*, 129176.

Millington, R., & Quirk, J. (1961). Permeability of porous solids. *Transactions of the Faraday Society*, *57*, 1200-1207.

Palandri, J. L., & Kharaka, Y. K. (2004). *A compilation of rate parameters of water-mineral interaction kinetics for application to geochemical modeling* (2331-1258).

Parkhurst, D. L., & Appelo, C. (2013). Description of input and examples for PHREEQC version 3—a computer program for speciation, batch-reaction, one-dimensional transport, and inverse geochemical calculations. *US geological survey techniques and methods*, *6*(A43), 497.

Plummer, L. N., Wigley, T. M. L., & Parkhurst, D. L. (1978). Kinetics of calcite dissolution in CO_2-water systems at 5 °C to 60 °C and 0.0 to 1.0 ATM CO_2. *Am J Sci*, *278*(2), 179-216.

Pokrovsky, O. S., & Schott, J. (2001). Kinetics and mechanism of dolomite dissolution in neutral to alkaline solutions revisited. *American journal of science*, *301*(7), 597-626.

Sherman, L. A., & Barak, P. (2000). Solubility and dissolution kinetics of dolomite in Ca–Mg–HCO_3/CO_3 solutions at 25 C and 0.1 MPa carbon dioxide. *Soil Science Society of America Journal*, *64*(6), 1959-1968.

Vespo, V. S. (2024). *Chemo-hydro-mechanical effects of CO_2 storage on Italian reconstituted caprock* Ph.D. Thesis. Politecnico di Torino. https://hdl.handle.net/11583/2993910

Vespo, V. S., Fiorucci, A., & Musso, G. (2025). *Chemo-mechanical effects of carbonates dissolution on a Carbonate Clay* International Conference on Energy Geotechnics, Paris. https://hal.science/hal-05343936v1

Vespo, V. S., Messori, A., & Musso, G. (2024). Threshold capillary pressure of caprocks for CO_2 storage: Numerical insight on the dynamic and residual method. *International Journal of Greenhouse Gas Control*, *135*. https://doi.org/10.1016/j.ijggc.2024.104135

Vilarrasa, V., Carrera, J., & Olivella, S. (2013). Hydromechanical characterization of CO_2 injection sites. *International Journal of Greenhouse Gas Control*, *19*, 665-677.

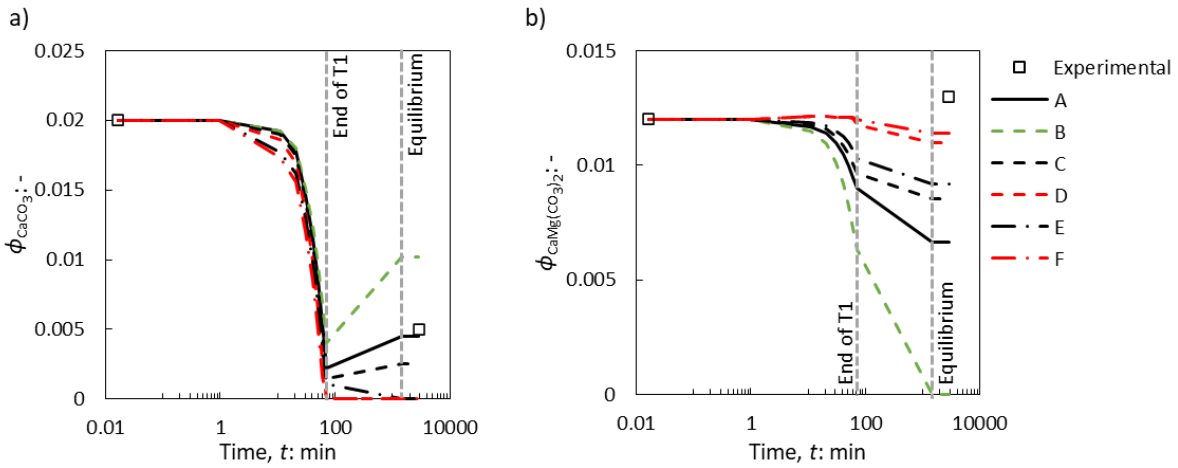

315

316 *Fig. 1 - Numerical time evolution of the volumetric fraction of calcite (a) and dolomite (b) in the T1 titration*
317 *tests and subsequent 48 hours of sedimentation for different equilibrium constants*
318 *(S_{CaCO_3} =$S_{CaMg(CO_3)_2}$ = 3·10⁶ m⁻¹)*

319

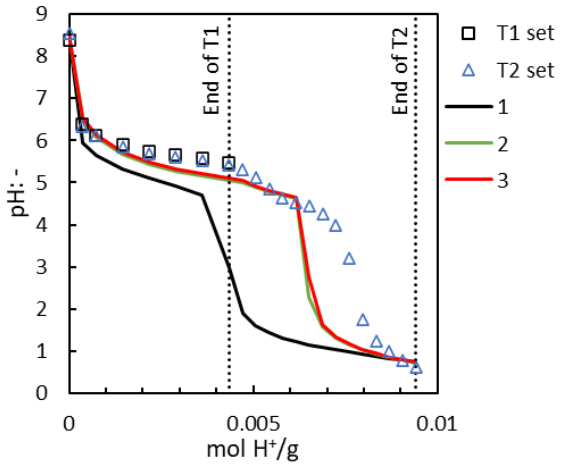

320

321 *Fig. 2 - Titration curves and numerical predictions for different reactive specific surface of calcite and dolomite*
322 *($K_{eq,CaCO_3}$ = 5.8·10⁻⁹, $K_{eq,CaMg(CO_3)_2}$ = 3.2·10⁻¹⁸)*

323

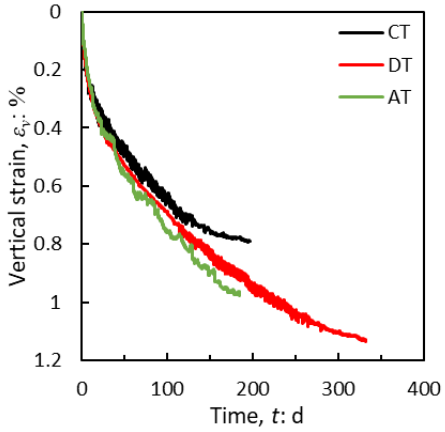

324

325 *Fig. 3 – Experimental time evolution of the vertical strain of the exposure stage (Diffusion Test (DT) and*
326 *Advection Test (AT)) and of the creep stage (Creep Test (CT))*

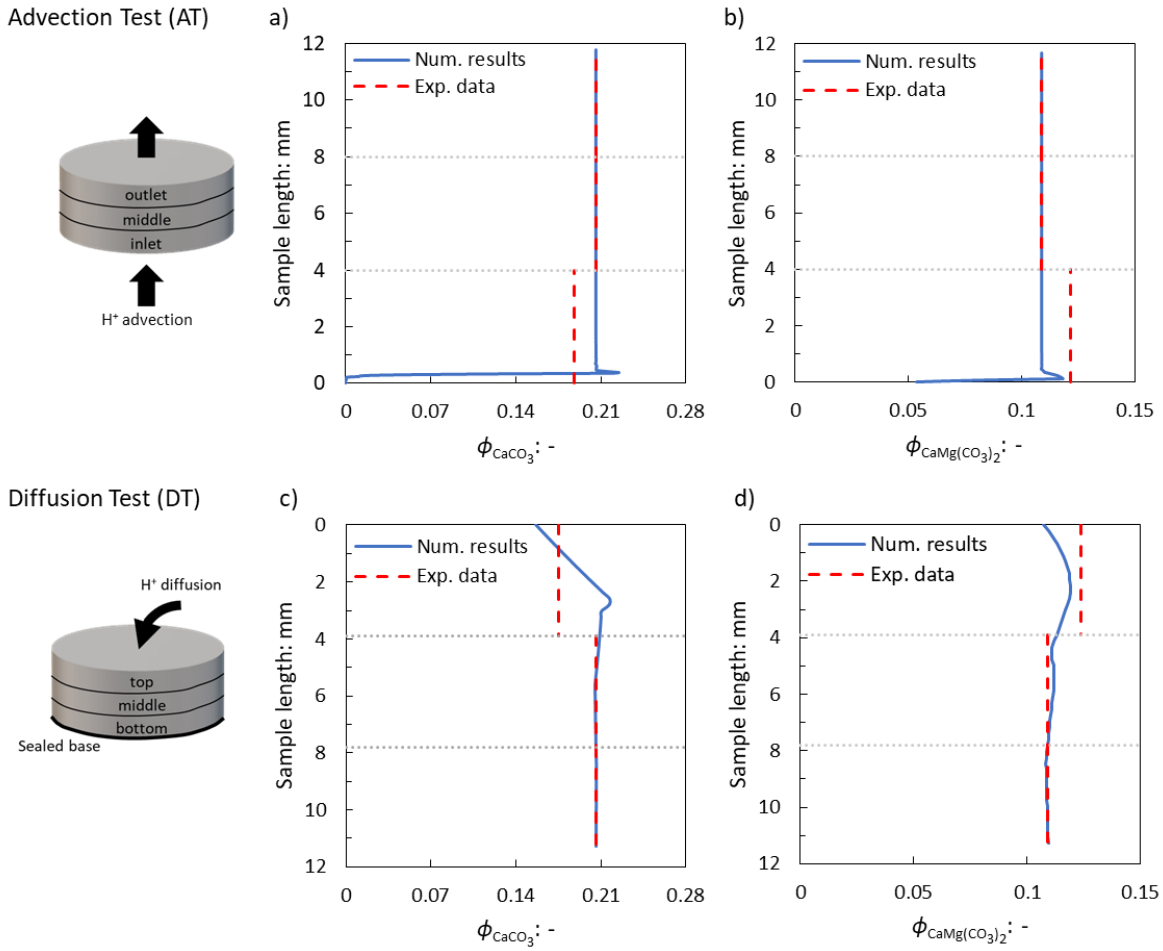

Fig. 4 - Profile along the specimen of the volumetric fraction of calcite (a) and (c), and dolomite (b) and (d), at the end of the Advection Test and Diffusion Test of 10^{-3} M HCl solution: comparison between experimental data and numerical results.

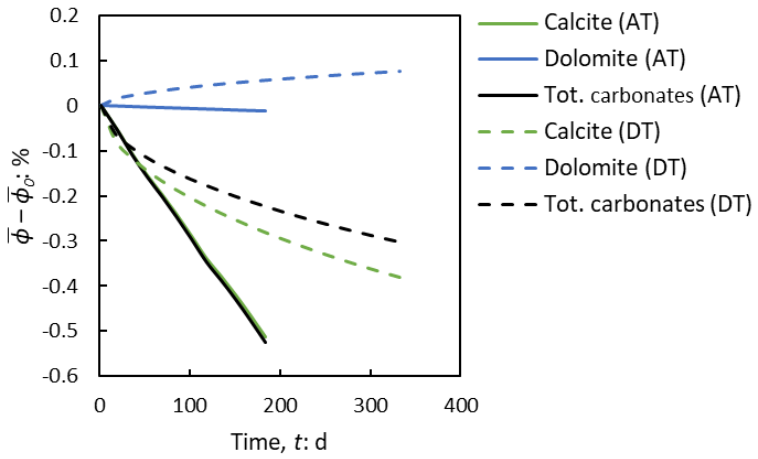

Fig. 5 - Time evolution of the average model-predicted carbonate volumetric fractions in the Advection Test (AT) and in the Diffusion Test (DT)

Table 1 - Calcite and dolomite reaction pathways

Calcite reaction pathway		Dolomite reaction pathway	
$CaCO_3 + H^+ \rightleftharpoons Ca^{2+} + HCO_3^-$	Eq. I	$CaMg(CO_3)_2 + 2H^+ \rightleftharpoons Mg^{2+} + Ca^{2+} + 2HCO_3^-$	Eq. IV
$CaCO_3 + H_2CO_3^* \rightleftharpoons Ca^{2+} + 2HCO_3^-$	Eq. II	$CaMg(CO_3)_2 + 2H_2CO_3^* \rightleftharpoons Mg^{2+} + Ca^{2+} + 4HCO_3^-$	Eq. V
$CaCO_3 \rightleftharpoons Ca^{2+} + CO_3^{2-}$	Eq. III	$CaMg(CO_3)_2 \rightleftharpoons Mg^{2+} + Ca^{2+} + 2CO_3^{2-}$	Eq. VI

Table 2 - Equilibrium constants and root mean square error of the numerical cases shown in Figure 1

Cases	$K_{eq,CaCO_3}$	$K_{eq,CaMg(CO_3)_2}$	RMSE
A	$4.6 \cdot 10^{-9}$	$3.2 \cdot 10^{-18}$	0.0076
B	$5.8 \cdot 10^{-9}$	$3.2 \cdot 10^{-17}$	0.0072
C	$5.8 \cdot 10^{-9}$	$3.2 \cdot 10^{-18}$	0.0063
D	$5.8 \cdot 10^{-9}$	$3.2 \cdot 10^{-20}$	0.0078
E	$7 \cdot 10^{-9}$	$3.2 \cdot 10^{-18}$	0.0065
F	$7 \cdot 10^{-9}$	$3.2 \cdot 10^{-20}$	0.0075

Table 3 - Reactive specific surfaces of the numerical cases shown in Figure 2

	1	2	3
S_{CaCO3} (m^2/m^3)	$3 \cdot 10^4$	$3 \cdot 10^6$	$3 \cdot 10^9$
$S_{CaMg(CO3)2}$ (m^2/m^3)	$3 \cdot 10^4$	$3 \cdot 10^6$	$3 \cdot 10^9$